3

Fabrication of a Nanosensor for Monitoring Health: Detection of Carbon monoxide and Acetone

This chapter explores the fabrication of nanosensors for detecting harmful gases critical to human safety. It highlights the development of cost-effective techniques for fabricating room-temperature nanosensors specifically designed for detecting carbon monoxide (CO) and acetone. The approach integrates commercially available substrates, such as PI and PET, with advanced nanostructures synthesized through an aqueous synthesis route. These nanosensors achieves high sensitivity and selectivity, representing a significant advancement in nanosensor technology for health monitoring applications.

3.1 ROOM TEMPERATURE OPERATED FLEXIBLE La-ZnO/MWCNTs SENSOR FOR PPB LEVEL CARBON MONOXIDE DETECTION

In this research, an interdigitated electrodes (IDEs) (thickness: 300 μm and spacing: 300 μm) were prepared using a laser carbonation technique on flexible polyimide substrate to prepared a high-performance flexible sensor. Here, Lanthanum (La)-Zinc Oxide (ZnO)/Multi-walled carbon nanotubes (MWCNTs) composites were successfully fabricated as sensing materials and loaded on a flexible polyimide for developing a room temperature CO gas sensor.

3.1.1 Introduction

Carbon monoxide (CO) is a gas that is exceedingly dangerous to human blood; once it has entered the human bloodstream through breathing, it binds to hemoglobin, and this inhibits hemoglobin from forming links with oxygen, which leads to hypoxia and, ultimately death from asphyxia (Farea et al., 2022). CO is an odorless and toxic gas produced mostly by partial fuel burning, making it difficult to detect (Yan Wang et al., 2020; Dongzhi Zhang et al., 2019). Generally, metal oxides (MO_x) are employed to fabricate such sensor that works at high temperatures (Gupta et al., 2013). As a result, considerable research has been conducted on low-temperature sensing materials for gas detection. Zinc oxide (ZnO) is a low-cost, bio-friendly, III-VI semiconductor with a wide bandgap that has found its way into a variety of every day and high-technology domains. In MO_x gas sensing, variations in surface defects, surface area, and bandgap caused by the introduction of dopants play an important role.

MOx-based gas sensors typically operate at higher temperatures (>100°C), thereby increasing their energy consumption, device size, and cost significantly. Furthermore, working at a higher temperature may cause changes in the microstructure of the sensing materials, resulting in decreased sensing performance. As a result, gas sensors operated at room temperature (RT) are more favorable, as they reduce energy usage and costs, allow device miniaturization, and are suitable for portable applications. Previously, many researchers modified the MOx surface with transition noble metals (Cu, Pd, Pt), rare earth metals (La, Rh, Eu), carbon materials, and composites materials, which prove to greatly enhance the response and selectivity of a gas sensor (Sheshkar et al., 2022). Additional atoms alter the gas sensor's characteristics by altering the morphology and energy band structure, as well as producing more active sites for gas interactions on the MO_x material's surface (Santhosam et al., 2020). Previously published research articles suggested that adding rare earth metals as dopants to MO_x materials can significantly improve their gas-sensing properties. Among the various Rare earth metal, La-

doped MO_x stands out due to its exceptional gas sensitivity, which has been validated through studies using various synthesis methods (Suo et al., 1997; Suzuki et al., 2020). For example, Kai et al. conducted experiments with La_{1-x}-Sr_x doped FeO_3 based sensor and observed a response of 11 min and recovery times of 15 min for a CO_2 concentration of 2000 ppm (Fan et al., 2013). Similarly, Marsal et al. successfully developed a screen-printed thick film CO gas sensor using La-SnO_2, which operated effectively at 200°C for CO concentrations ranging from 50 to 2500 ppm (Marsal et al., 2003). Despite these significant advances, the best combination of La-doped MOx materials for achieving RT sensing capabilities remains unexplored.

Furthermore, the use of carbon nanotubes (CNTs) in gas sensors provides a significant advantage over traditional MO_x sensors. While MO_x gas sensors typically require operating temperatures of 250 °C or higher, CNT-based gas sensors have the remarkable ability to detect a wide range of harmful gases at ambient temperature, including CO, H_2S, H_2, NO_2, NH_3, and CO_2. Adsorption/desorption of molecules of target gas that give or remove electrons on the surface of CNTs is well known to transfer electrons due to the electronic potential differences between the two materials, which resulted in the change in resistance of CNTs based gas sensors. By adding conducting polymer, metals, and MO_x, the selectivity of an MWCNT-based gas sensor can be improved. For example, Abdelhelim et al. demonstrated the fabrication of an ambient temperature operated CNT-based gas sensor array modified with 1.5, 1.0, and 0.2 nm of Au, Cr, and Pd metals, respectively (Abdelhalim et al., 2015). As a result, a ternary composite made of rear earth metal, MOx, and carbonous materials may attract a lot of interest in terms of improving the performance of RT sensing applications. In the current work, two composites, La-ZnO, and La-ZnO/MWCNTs based sensing materials, were synthesized by using a co-precipitation approach. This work aimed to investigate the viability of using these composites in the detection of CO at ambient temperature on a flexible PI substrate.

3.1.2 Experimental Section

Chemical reagents such as lanthanum nitrate ($LaNO_3$), multi-walled carbon nanotubes (MWCNTs) with a diameter of ~50 nm, methanol (CH_3OH**)**, cetyltrimethylammonium ammonium bromide (CTAB), zinc acetate ($Zn(CH_3COO)_2.2H_2O$), were procured with AR grade from SIGMA ALDRICH.

(a) Synthesis of La-ZnO Composite

The La-ZnO composite was synthesized via the co-precipitation technique with $Zn(CH_3COO)_2.2H_2O$, $LaNO_3$, and CTAB as reducing and capping agents. 0.01 M $Zn(CH_3COO)_2.2H_2O$ is added to 50 mL CH_3OH, followed by adding 0.2 g of CTAB, then continuously stirred for 3 hours at RT to form a homogenous precursor solution. After that, 0.07 M $LaNO_3$ was added, which was ultrasonicated for 60 mins. At last, 3 M NaOH was added in drops till the pH reached 12. The resulting solution was aged for 60 mins before being collected and cleaned with DI water to eliminate any residual reagents. Lastly, the collected slurry was heat treated at 80˚C for 6 hours in an oven to produce the La-ZnO composites.

(b) Synthesis of La-ZnO/MWCNTs composite

0.01 M $Zn(CH_3COO)_2.2H_2O$ were added to methanol, followed by adding 0.2 g of CTAB, then continuously stirred for 3 hours at room temperature to form a homogenous precursor solution. After that, 0.07 M $LaNO_3$ and 0.03 M MWCNTs were added, which were ultrasonicated for 60 mins. At last, 3 M NaOH was added in drops till the pH reached 12. The resulting solution was aged for 60 mins before being collected and cleaned with ethanol and DI water to eliminate any residual reagents and calcinated to produce the La-ZnO/MWCNTs composites.

(c) Gas sensing setup

Figure 3.1 (b) depicts a diagrammatic representation of the gas sensing instrumentation. The sensing setup includes a power supply, a digital multimeter, a CO gas tank, a mass

flow controller (MFC), and an acquisition device for studying the sensing information. To prepare the sensor device, we first fabricated interdigitated electrodes (IDEs) of highly graphitized carbon on commercially available flexible polyimide sheets (commercial name: Kapton™ HN, Dupont, thickness: 125 ± 13 µm) by irradiation of an infrared laser beam in an engraving mode on a 10.6 µm CO_2 laser-engraving machine (ULS Versa Laser 3.50) (see Figure 3.1 (a-1)). The optimized parameters for the laser irradiation were 15.6 cm/s speed, 4.8 W power, and 1000 pulse per inch (PPI). The IDEs featured an electrode thickness of ~300 µm and inter-electrode spacing of ~300 µm (see Figure 3.1 (a-2)). The sensing material La-ZnO-based composite was drop-casted on the carbon IDEs. The connecting pad of the IDEs was connected to a digital multimeter (Keithley Instruments), and a constant of 0.5 V was applied to the sensor to measure the resistance changes. A vacuum pump can also be used to remove the contaminated air from the sensing chamber. All interference gases were mixed with 1% dry nitrogen for the study.

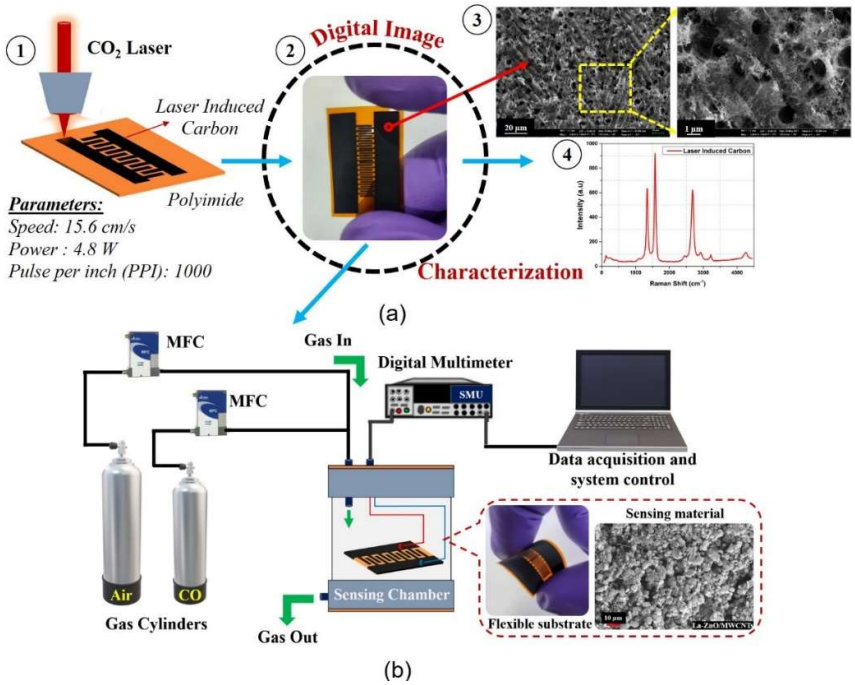


Figure 3.1: (a) The diagrammatic representation of the (1) fabrication of LIC electrode, (2) digital images of LIC electrode on Polyimide film, (3-4) Characterization: SEM and Raman results of LIC, and (b) the CO gas sensing instrumentation

3.1.3 Results and Discussions

(a) Morphological, elemental, and structural analysis of synthesized composite

Figure 3.1 (a-3) displays the SEM images of the PI sheets, which seem to have a low porous carbon structure. Increasing porosity is directly linked to gas release during laser graphitization (Correia et al., 2022). Higher laser power means more gas is released from the photothermal conversion, resulting in larger pore distribution and undesirably higher porosity in flexible sensors. Figure 3.1 (a-4) shows the raman spectroscopy of laser-induced carbon patterns used to evaluate their chemical structure. The spectra showed the three typical peaks of graphene-based materials at 1350, 1580, and 2700 cm^{-1}, which corresponded to the D, G, and 2 D peaks, respectively. The D peak is associated with the breathing modes of six-atom rings and is typically associated with the sample's level of defects, whereas the G peak is associated with the bond stretching of sp^2 pairs in both carbon rings and chains. The 2 D peak was caused by zone-boundary phonons of second order (Ferrari et al., 2006; Malard et al., 2009).

The surface morphology and elemental analysis of the synthesized La-ZnO-based composite were investigated using SEM and EDS techniques (see Figure 3.2). SEM imaging is one of the best techniques for investigating the particle shape, size, and surface arrangement of the composite, which was captured at magnifications ranging from 500 X to 5000 X with a 15 kV accelerating voltage. Figure 3.2 (a) depicts the porous spaces in between synthesized La-ZnO nanostructures, which aggregates to cause an improvement in the surface roughness of the composite. Moreover, the SEM image also shows the effect of stacking on the surface. The presence of MWCNTs increased the number of adsorption sites, allowing for direct interaction between La and ZnO to speed up gas sensing (see Figure 3.2 (b)). In addition, the carbon nanotube diameter is ~50 nm, which further increases the S/V ratio of the composite. Figure 3.2 (c, d) depicts the EDS spectrum used to analyze the chemical composition of the La-ZnO-based composite. The EDS spectrum shows that the composite comprises zinc (Zn), lanthanum (La), oxygen (O), and carbon (C) elements. The even distribution of the Zn, La, and O elements in the La-ZnO composite with atomic ratios of 39.29, 9.18, and 51.43, respectively, is evident from Figure 3.2 (c). However, the addition of long-length MWCNTs causes non-uniform scattering of the C element at 0.02 keV on the composite's surface due to agglomeration (see Figure 3.2 (d)). The absence of other elements in the EDS spectrum indicates the purity of the synthesized composite, which is consistent with the XRD results.

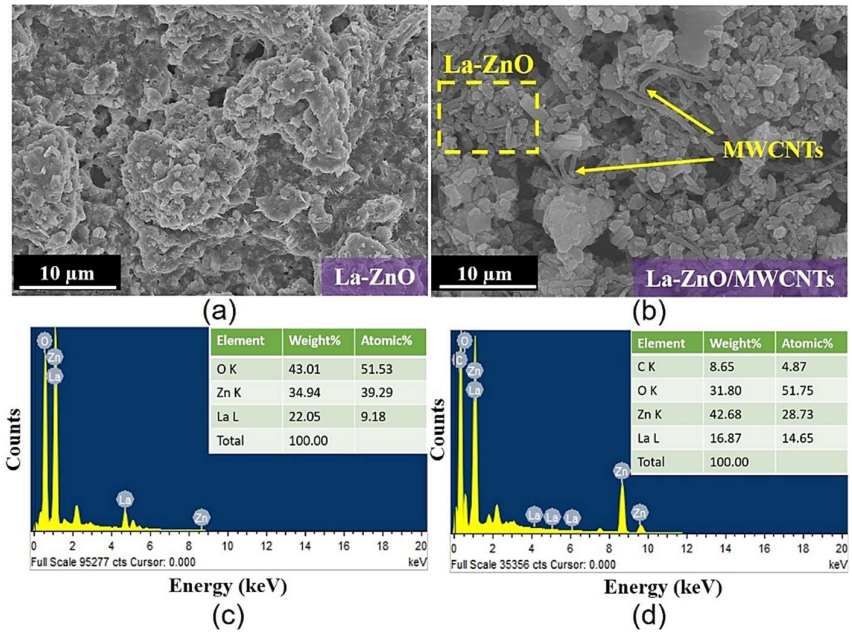


Figure 3.2: (a, b) SEM images, and (c, d) EDS images of synthesized La-ZnO and La-ZnO/MWCNTs composites

Figures 3.3 (a, b) show the XRD spectrum of La-ZnO based composites at ambient temperature, with 2θ ranging from 25˚ to 80˚ using Cu K1α radiation (1.54059 A˚). Various notable peaks for the plane were discovered in previous research, including (100) at 31.86˚, (002) at 34.54˚, (101) at 36.32˚, (102) at 47.62˚, (110) at 56.66˚, and (100) at 66.44˚. Similar peaks were also observed in the synthesized La-ZnO composite, which demonstrates good relevance to the standard JCPDS 36-1451 data file (Nguyen et al., 2019). As a result, the observed patterns strongly suggest the presence of a hexagonal wurtzite structure. Furthermore, the XRD spectra revealed that there was no formation of Zn–La alloys or lanthanum oxide (Arun Jose et al., 2012). As a result, it's assumed that the dopant is evenly distributed in the lattice of ZnO, causing no further changes in the crystal structure (Thi and Lee, 2017). Additional peaks of the diffraction peaks (002) at 26˚ and (100) at 43˚, corresponding to functionalized MWCNTs, were visible in the XRD spectrum of La-ZnO/MWCNTs (Rafique et al., 2022).

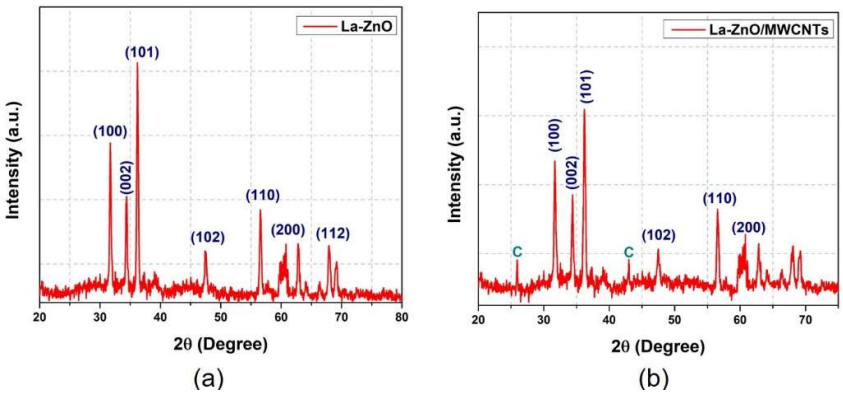


Figure 3.3: XRD spectrum of (a) La-ZnO, and (b) La-ZnO/MWCNTs composite

To identify chemical bonds and functional groups of La-ZnO-based composites, the FT-IR absorption analysis was performed (see Figure 3.4 (a, b)). The absorption spectrum at 573 cm^{-1} and 605 cm^{-1} is attributed to the Zn–O stretching vibration and La–O stretching, respectively (Salavati-Niasari et al., 2011). Adsorption peaks at 1210 cm^{-1}, 1274 cm^{-1}, 1553 cm^{-1}, and 1714 cm^{-1} were observed in the La-ZnO after the addition of MWCNTs, which correspond to the C-H, C=C, C-O, and C=O bands of a carboxylic group and bands of MWCNTs, respectively (Franco et al., 2019). The absorption of CO_2 on metal cations is revealed by the peak at 2330 cm^{-1} (Salman et al., 2019). The adsorption peak of the hydroxyl OH group from H_2O between 3414 and 3880 cm^{-1} induces the presence of molecules of water adsorption on the surface of La-ZnO/MWCNTs.

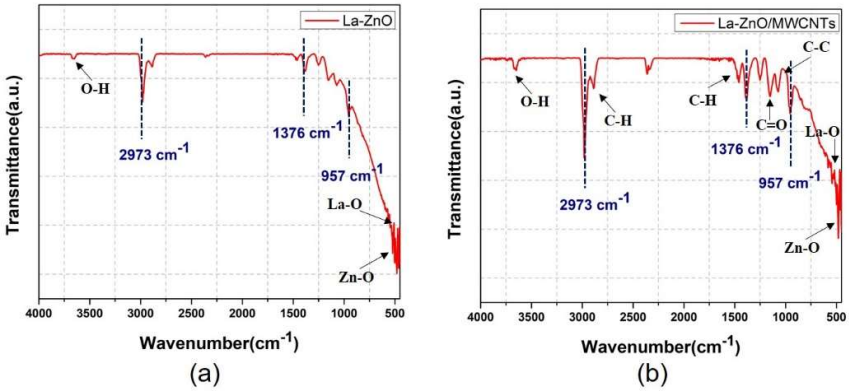


Figure 3.4: FTIR spectrum of (a) La-ZnO, and (b) La-ZnO/MWCNTs composite

The UV-Vis spectra investigation was carried out to examine the impact of La and MWCNTs doping on the electronic properties of ZnO. Figure 3.5 (a, b) depicts the UV-Vis spectra of the La-ZnO based composite. According to previous research, the absorption edge in ZnO at 300-350 nm is primarily due to the transfer of an electron from the valence band (VB) to the conduction band (CB) (Ahmad et al., 2020). While La-doped ZnO NPs show an absorption shift towards longer wavelengths, indicating metal incorporation, this could be due to the charge-transfer shift between the f-electrons of La metals and the formation of impurities state between the VB or CB of ZnO (Alam et al., 2018). The absorption peak of La-ZnO/MWCNTs is influenced by the characteristic absorption peak of La-ZnO, whereas MWCNTs have a very broad and featureless spectrum (Oppong et al., 2018). The absorption peak of the prepared composite exhibits a slight shift towards a longer wavelength, which is believed to be due to the defect initiated after the MWCNTs were added (Singh et al., 2011). This alters the lattice symmetry and, therefore, can change the band structure, resulting in significant shifts in their properties (Reddy et al., 2009). With the increase of concentration of MWCNTs, the concentration of charge carriers thereby increases, enhancing the states within the CB and attempting to push the Fermi level within the CB, resulting in the reduction of the energy gap. Furthermore, CTAB's

noncovalent modification of MWCNTs prevents the change in electronic energy levels of La-ZnO/MWCNTs composite

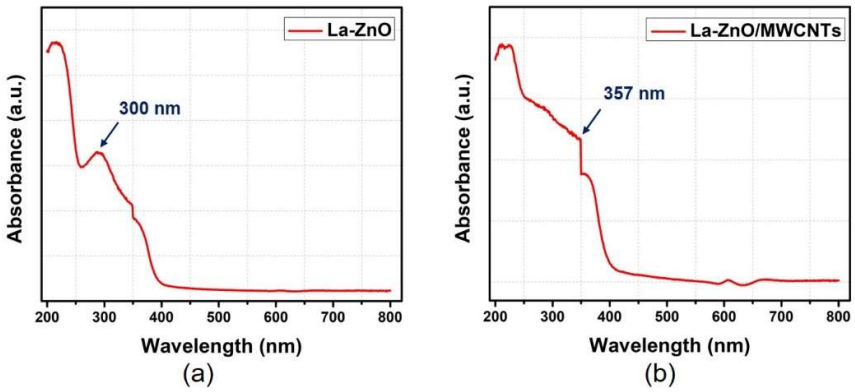


Figure 3.5: UV-Vis spectrum of (a) La-ZnO and (b) La-ZnO/MWCNTs composite

(b) Experimental Results: Gas Sensing Studies

Figure 3.6 (a, b) shows a response of synthesized La-ZnO and La-ZnO/MWCNTs composite to various concentrations of CO gas (100 ppb to 100 ppm) at 27˚C. As the gas is turned on, the sensor demonstrates good stability and reversibility because the resistance decreases rapidly to its minimum value and then returns to its initial value once the gas is turned off. However, the La-ZnO composite does not show any change to low concentration, i.e., 100 ppb to 1 ppm of CO gas. From figure 3.6 (c, d), it is clear that the response of the prepared La-ZnO nanocomposite does not show a response value towards 100 ppb CO gas at 27˚C, whereas the La-ZnO/MWCNTs have a response value of 1.08% at 100 ppb. The La-ZnO/MWCNTs based gas sensor satisfies the OSHA guidelines for a maximum permissible limit of CO gas exposure which is 50 ppm ("Occupational health guidelines for chemical hazards.," 2020). Our proposed sensor operates at various CO gas concentrations and has a detection limit of 100 ppb, implying that it can be used to detect CO gas early in hazardous environments where human health is at risk. The additions of MWCNTs results in a significant improvement in sensing characteristic. The La-ZnO/MWCNTs sensor had a maximum response value of 30.77% when exposed to 100 ppm CO, which was approximately 7.93 times higher than the La-ZnO-based sensor. This is because there was a greater availability of CO molecules at higher concentrations, which led to an effective reaction of gas molecules with the active sites of La-ZnO/MWCNTs. As a result, the response reveals an increasing trend as the gas concentration increases.

Numerous researchers have studied the detection of CO gas at ambient temperature using heterojunction materials in the past. For example, Lai et al. developed a room temperature operated sensor for CO gas detection based on a Pt and Pd decorated In_2O_3 nanocomposite produced on an Al_2O_3 substrate (Lai and Chen, 2012). The performance of a gas sensor is also determined by the response time and recovery time, which is defined as the time (90%) required by the sensor to attain a total change in resistance after switching ON/OFF the target gas (Duan et al., 2022; Y. Guo et al., 2023). The response kinetics of gas sensors are significantly affected by the chemical interactions and gas diffusion mechanisms that take place between the gas molecules and sensing material. In general, sensing materials with a large surface area allow for more gas diffusion pathways, resulting in a quick response and recovery behaviour (Sun et al., 2014). Moreover, increasing the reaction rate via increasing temperature will further result in faster response and recovery behaviors of a gas sensor. The La-ZnO sensor responds clearly to 100 ppm CO gas with response, response time, and recovery time of 3.88%, 1612.39 sec, and 3339.18 sec, respectively. Similarly, La-ZnO/MWCNTs based sensor displays a higher response of 30.77% to 100 ppm CO gas. Even at 100 ppb (Limit of Detection), the La-ZnO/MWCNTs sensor has a response, response time, and recovery time of 1.08%, 803 sec, and 1167 sec, respectively. The La-ZnO material has a sensitivity of 0.033%/ppm, whereas the La-ZnO/MWCNTs material

has a significantly higher sensitivity of 7%/ppm up to 1 ppm. The results conclude that the La-ZnO/MWCNTs sensor is a promising candidate for CO sensing.

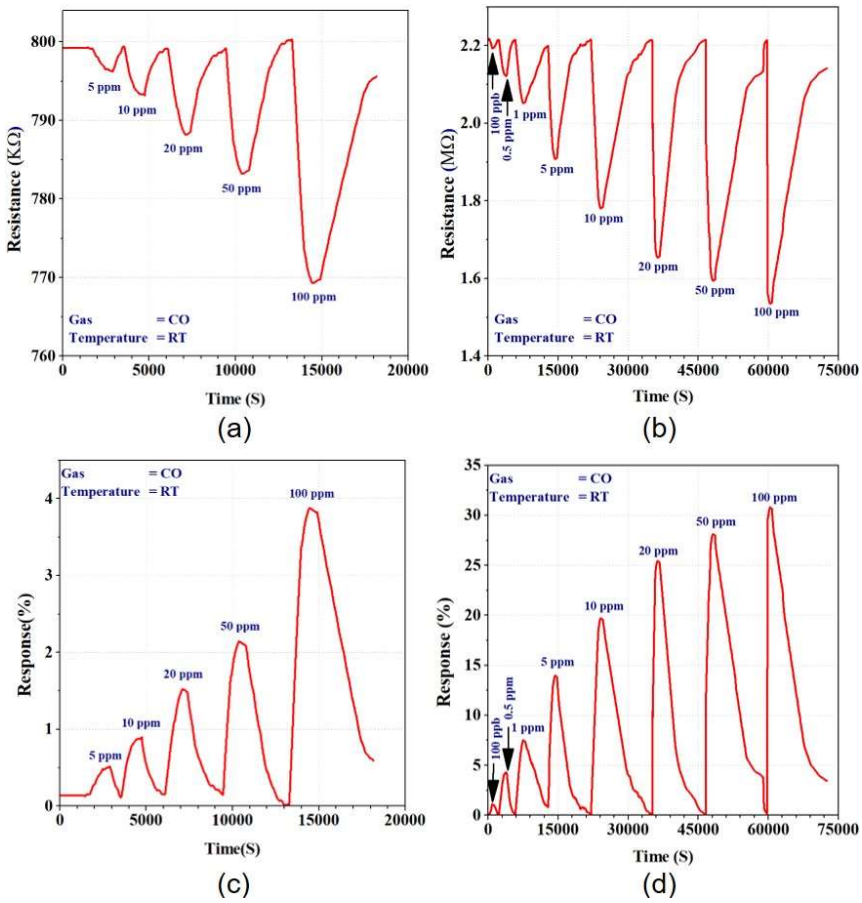


Figure 3.6: (a, b) The change in resistance vs. time graph and (c, d) response % vs. time graph for La-ZnO and La-ZnO/MWCNTs sensor, respectively

The evaluation of gas sensor performance can be enhanced by assessing humidity levels, which can improve their precision, dependability, and durability. To achieve this, we incorporated La-ZnO with intrinsically hydrophobic MWCNTs. MWCNTs are naturally hydrophobic due to their cylindrical shape, high S/V ratio, and the presence of hydrophobic groups (-CH_3, -CH_2-, and -C_6H_5). Figure 3.7 displays the response of La-ZnO/MWCNTs composite sensors to 20 ppm CO at 0-90% RH. These sensors exhibit anti-humidity characteristics, as evidenced by their response to humidity levels ranging from 0%-90%. Specifically, at 0%, 30%, 50%, 70%, and 90% RH, the sensor responses were 25.38%, 24.70%, 24.45%, 24.44%, and 22.06%, respectively. Even at 90% RH, the sensor exhibited a 13.081% decrease in response compared to 0% RH, indicating that it can be classified as a humidity tolerant sensor. Furthermore, a repeatability study is performed on the La-ZnO/MWCNTs sensor to investigate the sensor's behavior to maintain a consistent signal output across multiple test cycles. Figure 3.8 (a) depicts the repeatability behavior of a La-ZnO/MWCNTs sensor for 50 ppm CO gas. The result shows that the response is consistent across the three-cycle test. Figure 3.8 (b) depicts the response of both sensing materials to CO gas at various concentration levels ranging from 100 ppb to 100 ppm. The results clearly show that the La-ZnO/MWCNTs composite has a higher response value than the La-ZnO.

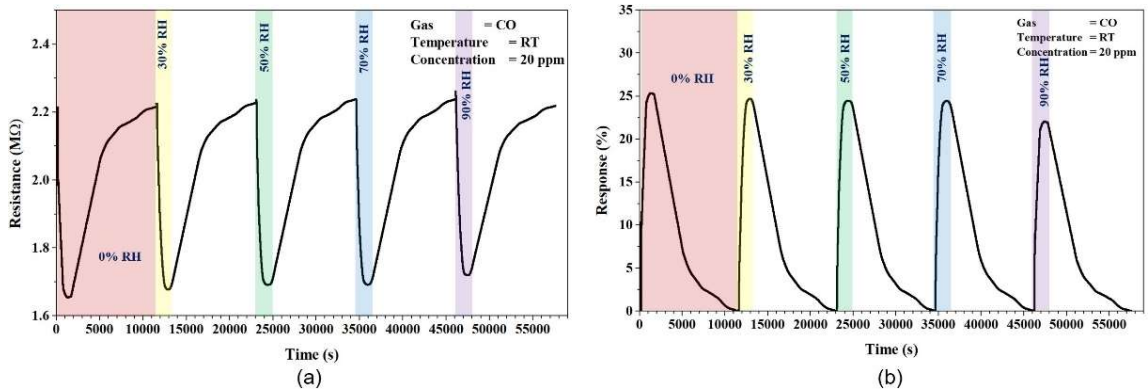


Figure 3.7: (a, b) The change in resistance vs. time graph and response % vs. time graph for La-ZnO/MWCNTs sensor at different relative humidity levels

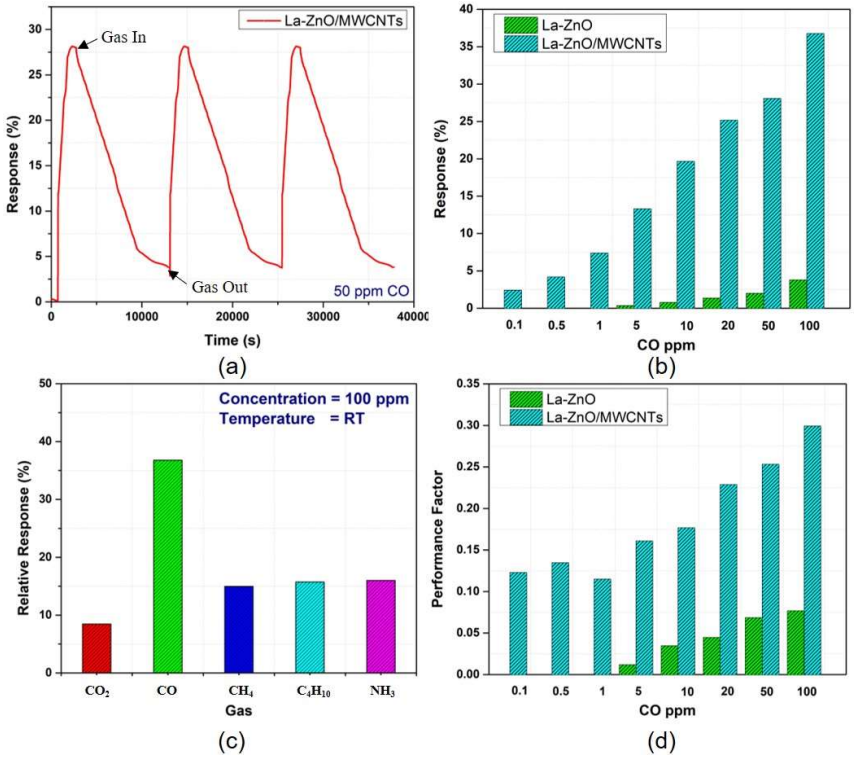


Figure 3.8: (a) A three-cycle repeatability test of La/ZnO/MWCNTs sensor at 50 ppm, (b) Response graph of both sensors at different concentrations of CO gas, (c) selectivity test of La-ZnO/MWCNTs sensor, and (d) performance factor study of both La-ZnO based sensor

In real-world applications, flexible gas sensors operating at room temperature must be able to distinguish between different gases. The selectivity of the La-ZnO/MWCNTs sensor was investigated in the presence of 100 ppm of interfering gases such as methane (CH_4), carbon dioxide (CO_2), butane (C_4H_{10}), and ammonia (NH_3). The maximum response of the La-ZnO/MWCNTs sensor to 100 ppm CO gas is shown in Figure 3.8 (c). The relative response % for CO_2, CH_4, C_4H_{10}, and NH_3 is found to be 8%, 17%, 18%, and 17%, respectively, which are much lower compared to CO (~30.77%). Among the other interfering gases investigated, CO was found to be a strong reducing agent that efficiently removes the adsorbed oxygen present on the surface of the La-ZnO/MWCNTs sensor, resulting in high selectivity. Moreover, a bending test on the sensor before and after bending is also investigated at 20 ppm of CO gas. The results show a negligible change in the sensing response of La-ZnO/MWCNTs. The performance factor is another criterion that is used in the process of determining the efficiency of the gas sensor. The performance factor is defined as the ratio of sensitivity to total cycle time (response and recovery

time). Figure 3.8 (d) shows the performance factor of both gas sensors. The result indicates the best performance of La-ZnO/MWCNTs sensors at 100 ppm of CO gas.

(c) Sensing mechanisms

The chemiresistive gas sensor is primarily based on (a) chemical reactions and (b) gas adsorption on sensing materials' surfaces (Yamazoe and Shimanoe, 2008; Yiqun Zhang et al., 2018). When ZnO is exposed to air, oxygen molecules bind to its surface and capture the CB electron, and subsequently, O_2^- ions are formed (at RT), leading to the development of the electron depletion layer (EDL). Under the exposure of CO gas, EDL acts as a potential barrier between adjacent grains, increasing sensor resistance. The lower the number of electrons in the CB, the higher the surface potential barrier and, thus greater the resistance.

$$O_{2(gas)} \leftrightarrow O_{2(adsorbed)} \rightarrow O_{2(adsorbed)} + e^-_{ZnO} \rightarrow O^-_{2(adsorbed)} \tag{4.1}$$

When reducing gases such as CO are introduced, they quickly react with the oxygen ions, releasing electrons back to the CB of ZnO, resulting in the decrease of EDL and lowering the resistivity.

$$2CO + O^-_{2(adsorbed)} \rightarrow 2CO_2 + e^-_{ZnO} \tag{4.2}$$

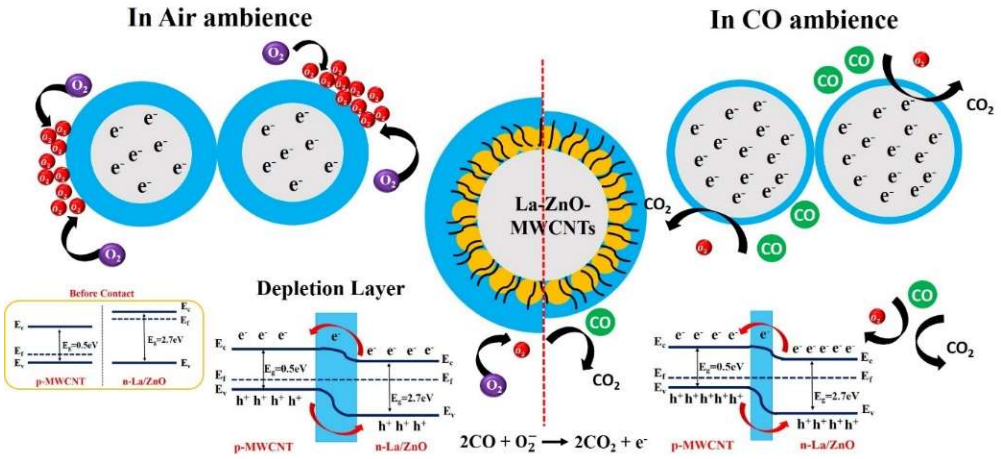


Figure 3.9: Schematic view of sensing mechanisms of La-ZnO/MWCNTs

Multiple approaches were used to improve the response and cross-selectivity of ZnO based sensors. The functionalization of ZnO with metal catalysts is one of the commonly used approaches to enhance the efficiency of chemiresistive sensors. At room temperature, La metal incorporated into ZnO exhibit excellent sensitivity. The carrier concentration of $O^-_{2(adsorbed)}$ ions in La cause a drastic change in resistivity when exposed to CO gas. The primary factors for improving CO response properties of La-doped ZnO can be described as (a) enhanced chemisorption, (b) spill-over effects, and (c) generation of active reaction sites (Jeong et al., 2016; S. Tian et al., 2015; Venkatesh et al., 2014). Furthermore, the increased oxygen vacancies, as well as other defects caused by La doping, provide more active sites for reactions, hence enhancing the CO gas response of the La-ZnO composite. The energy band gap values of ZnO and La-ZnO are important. The energy band gap of ZnO is 3.37 eV, while the energy band gap of La-ZnO decreases (with the incorporation of La) to 2.7 eV. Similar research conducted by Ahmed et al. (Ahmed et al., 2019) reported that the energy band of ZnO decreases with La doping. This decrease occurs because the ionic radii of Zn^{2+} and La^{3+} ions are significantly different, resulting in crystal defects in ZnO. These crystal defects generate new localized states around the CB, allowing free electrons to transition from the VB to the defects band rather than directly to the CB. Therefore, it can be inferred that the sensing performance is significantly influenced by the

La-ZnO surface. Furthermore, MWCNTs serve as a framework for the formation of La-ZnO nanoparticles, which aids in the efficient transfer of electrical charges within the system (refer to Figure 3.9) (Özütok et al., 2019a). The MWCNTs possess an extensive specific surface area due to their hollow structure, resulting in a high number of exposed reaction sites. However, their strong sp2 bonding renders them chemically inert. Consequently, the functionalization of La-ZnO with MWCNTs undoubtedly enhances chemical reactivity, thereby promoting increased adsorption of oxygen on the composite surface (Abraham et al., 2019). Besides, La-ZnO is covered by MWCNTs, allowing the formation of p-n heterojunctions due to MWCNTs' higher work function than ZnO (Hojati et al., 2018). This leads to the transfer of electrons from ZnO and holes from MWCNT until the built-in potential inhibits the further transfer of both electrons and holes (Kwon et al., 2017). The larger depletion region and high surface area of ZnO/MWCNTs composite sensors are the reasons for the increased sensitivity. Because MWCNTs have a high S/V ratio, their incorporation increases the surface area. Moreover, by incorporating MWCNTs into La-ZnO, the depletion region is expanded, allowing the larger specific surface area to absorb more gas molecules on the surface, similarly as reported by Portirak et al. (Potirak et al., 2013). Electrons move freely on the surface of MWCNTs due to π-bonding tends to result in an expansion of the depletion region. As a result of these factors, the amount of oxidation and reduction reactions occurring on a specific surface increases, resulting in a rapid movement of surface electrons (Özütok et al., 2019b). Table 3.1 shows a comparative analysis of the La-ZnO/MWCNTs sensor with the previously published articles.

Table 3.1: A comparison of recently published papers on different composite materials (ZnO and MWCNTs) for carbon monoxide gas detection

Sensing materials	CO Gas (ppm)	Temperature (°C)	Response (%)	Ref
MWCNTs/PDDA	1-20	25	-	(Roy et al., 2020)
ZnO/MWCNTs	50	70	13	(Hojati et al., 2018)
PANI/MWCNTs	500-1000	27	6.8	(Roy et al., 2018)
Au/ZnO	50	25	55.3	(Arunkumar et al., 2017)
CNT/Au/SnO_2	500-2500	27	70	(Du et al., 2008)
Pt/ZnO	50	180	3.57	(Yan Wang et al., 2020)
La-ZnO/MWCNTs	100 ppb	27	1.08	Current Work

3.1.4 Summary

In this study, rare earth metal doped ZnO-MWCNTs composites were synthesized using a co-precipitation technique and then loaded onto a flexible polyimide (PI) substrate for CO gas detection. Room temperature operated gas sensors are highly desirable, but currently, available gas sensors suffer from these flaws. At 27°C, the prepared La-ZnO/MWCNTs sensor responded 7.93 times faster than La-ZnO to 100 ppm CO gas. The response of the La-ZnO/MWCNTs composite sensors to 20 ppm CO was tested at six different relative humidity (RH) levels ranging from 0% to 90% in increments of 20% RH. These sensors had humidity tolerant properties, as evidenced by their responses to different humidity levels. Even when exposed to 90% RH, the sensor only showed a 13.081% reduction in response compared to 0% RH, indicating that it is a humidity tolerant sensor. Furthermore, the La-ZnO/MWCNTs sensor had good selectivity and could detect low CO concentrations of 100 ppb. As a result, the proposed high-performance flexible sensor has a lot of potential for use in wearable devices to sense CO gas at room temperature for trace level detection.

3.2 FLEXIBLE MWCNTs/Nb_2O_5 HYBRID BREATH SENSOR FOR THE NON-INVASIVE DETECTION OF EXHALED DIABETES BIOMARKER

This study introduces a novel room temperature operated flexible acetone sensing platform, leveraging a hybrid material composed of multi-walled carbon nanotubes (MWCNTs) and niobium oxide (Nb_2O_5). The platform demonstrates sensitivity and selectivity towards acetone, a prominent biomarker of diabetes, offering promise for real-time health monitoring applications. Additionally, the sensor's characteristic features were collected, and four different machine learning (ML) algorithms were applied to visualize and classify the gases with good quantifications. Furthermore, regression modelling was also used to quantitatively predict the gas concentration. In addition, the sensor was tested to distinguish between signals from simulated diabetic and healthy breath samples. These sensing performances indicate that the breath sensor has practical applications that could potentially provide a non-invasive monitoring method for diabetic patients.

3.2.1 Introduction

Diabetes mellitus, a chronic metabolic disorder characterized by elevated blood glucose levels, poses significant challenges to global public health. Effective management of diabetes relies heavily on continuous monitoring of blood glucose levels, traditionally achieved through invasive methods such as fingerstick testing. However, the pursuit of non-invasive monitoring approaches has gained traction due to their potential to enhance patient compliance and quality of life. Among emerging non-invasive techniques, the analysis of exhaled breath biomarkers presents a promising avenue for real-time monitoring and early detection of diabetes-related metabolic changes. Gas sensors can be potential solution to this problem and can play a crucial role in modern advanced devices, allowing swift monitoring, detection, and regulation of gas mixtures and vapors in the surrounding environment (C. Li et al., 2022). Among the gases, acetone, a common volatile organic compound (VOC), is widely used in industries, households, medicine, and various other fields (D. Zhang et al., 2014). However, owing to its high volatility, acetone inhalation poses significant health risks (Benamara et al., 2023). Even at concentrations of several hundred parts per million (ppm), it can lead to headaches, respiratory issues, dizziness, and other adverse effects (J. Li et al., 2022). The rapid detection and precise measurement of ultralow concentrations of acetone vapor (ranging from 0.7 to 5 ppm) play a pivotal role in designing cutting-edge medical diagnostic systems (Španěl et al., 2011). Analyzing human exhaled breath offers a non-invasive approach for detecting and investigating specific diseases. Notably, even minor fluctuations in acetone levels within the exhaled breath can signal the presence of diabetes. Furthermore, acetone is a crucial raw material for organic synthesis in modern industrial processes; however, high concentrations of acetone can pose risks in the workplace, including explosive accidents and irreversible damage to humans. To address this critical need, the development of highly selective, rapid, and sensitive acetone detectors with nanoscale structures is essential. Further, wearable flexible acetone sensors provide continuous, real-time monitoring of acetone concentrations. Their flexibility ensures wearer comfort and unobtrusiveness, making them suitable for medical diagnostics and environmental safety applications.

The sensitivity and reliability of gas sensors are enhanced by the interactions between the gas molecules and the sensing material, which are influenced by the available active surface area. This can further enhance the specificity of the sensor, allowing it to distinguish between different gas types based on their chemical properties. Numerous reports have discussed the sensing performance of nanostructured metal oxides (MO_x), yet relatively few studies have explored the feasibility of transition MO_x, such as Nb_2O_5, for gas sensing. Nb_2O_5, a wide bandgap n-type metal oxide, has desirable properties such as excellent chemical stability, low film stress, and a high refractive index (n = 2.4 at 550 nm) (Xiao et al., 2008). The intercalation reactions of Nb_2O_5 are highly sensitive to the preparation temperature and particle size. Nb_2O_5 exhibits various polymorphic forms depending on the preparation temperature (Le Viet et al., 2010), including

orthorhombic, tetragonal, pseudo-hexagonal, and monoclinic phases. Owing to its remarkable properties, Nb_2O_5 is utilized in a range of applications, such as catalysis, batteries (Ramakrishna et al., 2010), solar cells (H. Zhang et al., 2012), and optical sensors (Ab Kadir et al., 2015). Several synthesis methods have been reported to obtain nanostructured Nb_2O_5, including sol–gel dip-coatings (Habibi and Mokhtari, 2012), hydrothermal (Wen et al., 2011), pulsed laser deposition (Ghosh et al., 2011), and electrodeposition (Zhitomirsky, 1998). Recently, researchers have focused on the preparation of Nb_2O_5 nanostructures for sensing applications. Moreover, Nb_2O_5 nanowire arrays show moderate sensing performance of the prepared hydrogen sensor at room temperature (Hyodo et al., 2009). Similarly, Mirzaei et al. developed an ambient-temperature hydrogen sensor using a NiO/Nb_2O_5 hybrid composite via a hydrothermal method (Mirzaei et al., 2017). The NiO/Nb_2O_5 hybrid composite showed a response (1.68%) to 500 ppm H_2 compared to that of pristine Nb_2O_5. As demonstrated in this study, pristine Nb_2O_5 shows low responses to the target gas at room/low temperatures. Many other approaches have been used to develop metal-oxide heterostructures to improve the sensing performance of devices at room/low temperatures. Over the years, researchers have focused on carbon-based materials for gas sensing applications. Among these, CNTs stand out for their exceptional electrical and mechanical characteristics and low-temperature operation, making them ideal for the development of highly sensitive and selective sensors. However, pristine CNTs lack the necessary selectivity and require surface functionalization to improve their performance. Significant efforts have been made to address this challenge, leading to the discovery that functionalized MWCNTs combined with various MO_x greatly enhance gas sensing capabilities (Bachhav et al., 2015).

Developing a room temperature acetone sensor for wearable and flexible breath sensing applications is a challenging endeavor that necessitates substantial research and development efforts. This study is focused on the fabrication of a flexible $MWCNTs/Nb_2O_5$ based gas sensor for detecting low concentrations of acetone at RT. Moreover, the practical utility of the sensor is evaluated by subjecting it to various healthy and simulated human breath samples, which could potentially provide a non-invasive monitoring method for diabetic patients.

3.2.2 Experimental Section

Chemical reagents such as Niobium chloride ($NbCl_2$), multi-walled carbon nanotubes (MWCNTs) with a diameter of ~50 nm, nitric acid (HNO_3), hydrogen peroxide (H_2O_2), acetone and polyethylene terephthalate (PET) substrate (thickness: 100 μm), were procured with AR grade from Sigma Aldrich.

(a) Preparation of Nb_2O_5 and $MWCNTs/Nb_2O_5$ Hybrid Sensing Materials

Nb_2O_5 NPs were obtained using a hydrothermal method (see Figure 3.10). Here, a 0.25 g $NbCl_2$ was added to diluted HNO_3 in order to avoid salt residual. Followed by the addition of 5 mL H_2O_2 in the above solution and magnetically stirred for 30 min to obtain a homogenous yellow coloured solution, which indicated the presence of water-soluble $Nb(O_2)^{4-}$ complex. After that, the 30 mL of DI water was added to the solution and transferred to the 50 mL autoclave for 22 hours at 110˚C. After the reaction, the precipitate was centrifuged at 7000 rpm for 5 mins and subsequently washed using acetone and DI water. The obtained slurry was then preheated at 90˚C for 6 hours, followed by calcination at 500˚C in a muffle furnace. Similarly, $MWCNTs/Nb_2O_5$ hybrid was prepared by adding 0.5 wt%, and 1 wt% MWCNT, just before transferring the solution to the autoclave. Further, all the steps remain as same as used for Nb_2O_5.

(b) Device Fabrication and Sensing Experiment

A standardized cleaning protocol was implemented to prepare the PET substrate prior to the deposition of electrodes. The substrate undergoes a sequential cleaning process involving the use of IPA and DI water to remove contaminants. After the cleaning process, the PET film was placed in a thermal evaporation system with a shadow mask, and 30/300nm Ti/Ag electrodes were deposited. Finally, the electrodes were coated with the sensing materials to fabricate the

final devices. An I-V curve is recorded in the sensing chamber at ambient temperature to check the development of the prepared device. A voltage of 2 V was applied to these IDEs, which were connected to a Keysight 29018B source-meter, to measure the variations in resistance of the prepared sensor under various concentrations of target gas (see Figure 3.11). Liquid VOCs were introduced into a sensing chamber using a micro-syringe. The VOCs evaporated rapidly due to the high vapor pressure of the liquid VOC. Moreover, a vacuum pump was employed to eliminate contaminated air from the sensing chamber. The static liquid-gas distribution method was used to determine the target gas concentration based on equation 4.3 (Malepe et al., 2023).

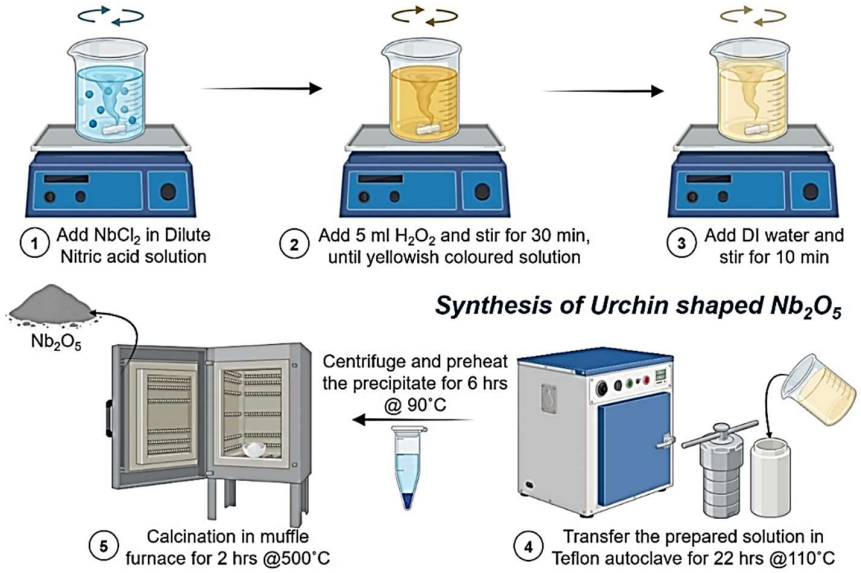


Figure 3.10: Schematic representation of step involved in the synthesis of Nb_2O_5

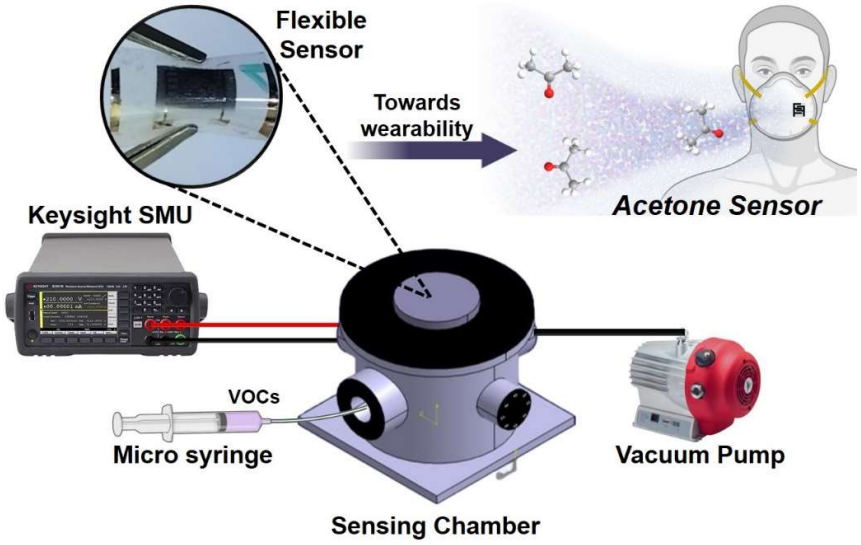


Figure 3.11: Schematic view of gas sensing setup with inset photograph of flexible MWCNTs/Nb_2O_5 device

$$C = \frac{22.4 \times \rho \times T \times V_s}{273 \times V \times M_r} \times 1000 \qquad (4.3)$$

where C (in ppm) represents the concentration, ρ (in g.cm^{-1}) and M_r is the density and molar mass of liquid VOCs, T (in K) is the temperature, V_s (in µL) and V (in L) is the volume of the injected VOCs and volume of the chamber, respectively. Further to test the sensor under practical conditions, the real breath samples of five healthy volunteers (aged between 20-30 years) were collected in the Tedlar bag, and the experiment was performed with their consent.

(d) Computational and Machine Learning (ML) Details

The ML code was developed using Jupyter Notebook (Python v6.4.8) within the Anaconda Navigator environment. The process utilized four essential libraries, including Pandas, NumPy, Scikit-Learn, and SciPy, for data preprocessing, model training, and testing. The programs were run on a computer equipped with an Intel(R) Core(TM) i5-10700 CPU running at 2.90 GHz. The extraction of features such as response time, recovery time, and response (%) from sensor data was carried out to distinguish different analytes, as these features provide useful information. This extracted data was subsequently utilized to train the ML models. For data visualization and dimensionality reduction, t-distributed Stochastic Neighbor Embedding (t-SNE) was used. Further, due to their proven effectiveness in handling small datasets with high accuracy, K-Nearest Neighbors (KNN), Support Vector Machines (SVM), Naive Bayes (NB), and Random Forest (RF), were selected for gas classification (Acharyya et al., 2020; Kulkarni et al., 2023). For quantifying gas concentrations, regression algorithms such as Linear Regression (LR), RF Regression (RF-R), KNN Regression, and SV Regression were used.

3.2.3 Results and Discussion

(a) Sensing Material Characterizations

The surface morphology of the hydrothermally synthesized Nb_2O_5 nanoparticles (NPs) is depicted in Figure 3.13 (a-c). The FESEM image displays interconnected Nb_2O_5 nanostructures with porous spaces in between, indicating the presence of Nb_2O_5 aggregations that may enhance surface roughness. Upon closer examination, the image confirms the successful synthesis of urchin-shaped Nb_2O_5 nanostructures. Further, the possible growth mechanisms of Nb_2O_5 are explained in Figure 3.12. Initially a $NbCl_5$ is added to a diluted HNO_3 solution. Subsequently, H_2O_2 was added to the solution to eliminate chloride ions via an oxidation-reduction process, which resulted in the appearance of a yellow solution indicating the formation of water-soluble $[Nb(O_2)_4]^{3-}$. Further, the presence of excess H_2O_2 led to the formation of amorphous hierarchical spheres of Nb_2O_5 and $Nb_2O_5 \cdot nH_2O$. Finally, annealing at 500°C resulted in the crystallization of Nb_2O_5, which favored pore coalescence due to the crystallisation of walls separating mesopores in their structures. Further, when 0.5 wt% and 1 wt% of MWCNT were incorporated into Nb_2O_5, a mixed morphology of the resulting hybrid was formed. As depicted in Figure 3.13 (d-f), FESEM images of 1 wt% MWCNT sample exhibit the presence of MWCNTs with a diameter of ~50 nm, which surround the urchin-shaped Nb_2O_5 NPs. Their unique morphology is expected to offer significant advantages in gas sensing due to their high surface area and structural characteristics. Further, this arrangement is expected to improve the S/V ratio of the hybrid by increasing the number of adsorption sites for gas molecules during the sensing process. Moreover, Figure 3.13 (g-h) displays the TEM images of Nb_2O_5 NPs and MWCNT/Nb_2O_5 hybrid. Figure 4.13 (g) depicts a high dispersion of Nb_2O_5 NPs with a size of ~15 nm, suggesting a well-organized crystal structure. Additionally, Figure 3.13 (h) displays a uniform distribution of numerous Nb_2O_5 NPs on the surface of MWCNTs. The addition of MWCNTs causes the surface of the MWCNTs/$Nb2O_5$ hybrid to contain carbon (C), resulting in the presence of C, Nb, and O elements (see Figure 3.13 (i-j)). The EDS and elemental mapping results confirmed the purity of the prepared hybrid, which aligns with the XRD results.

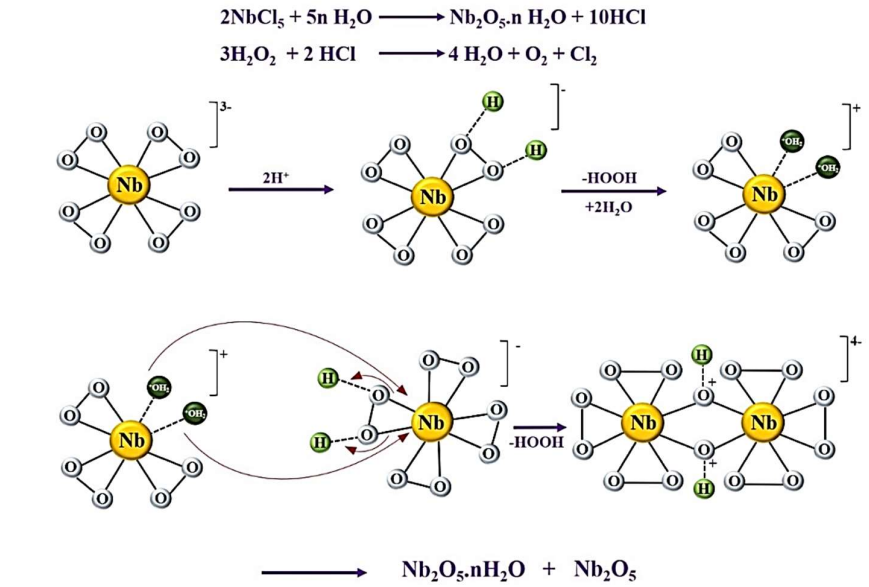


Figure 3.12: Possible growth mechanisms of urchin shaped Nb_2O_5

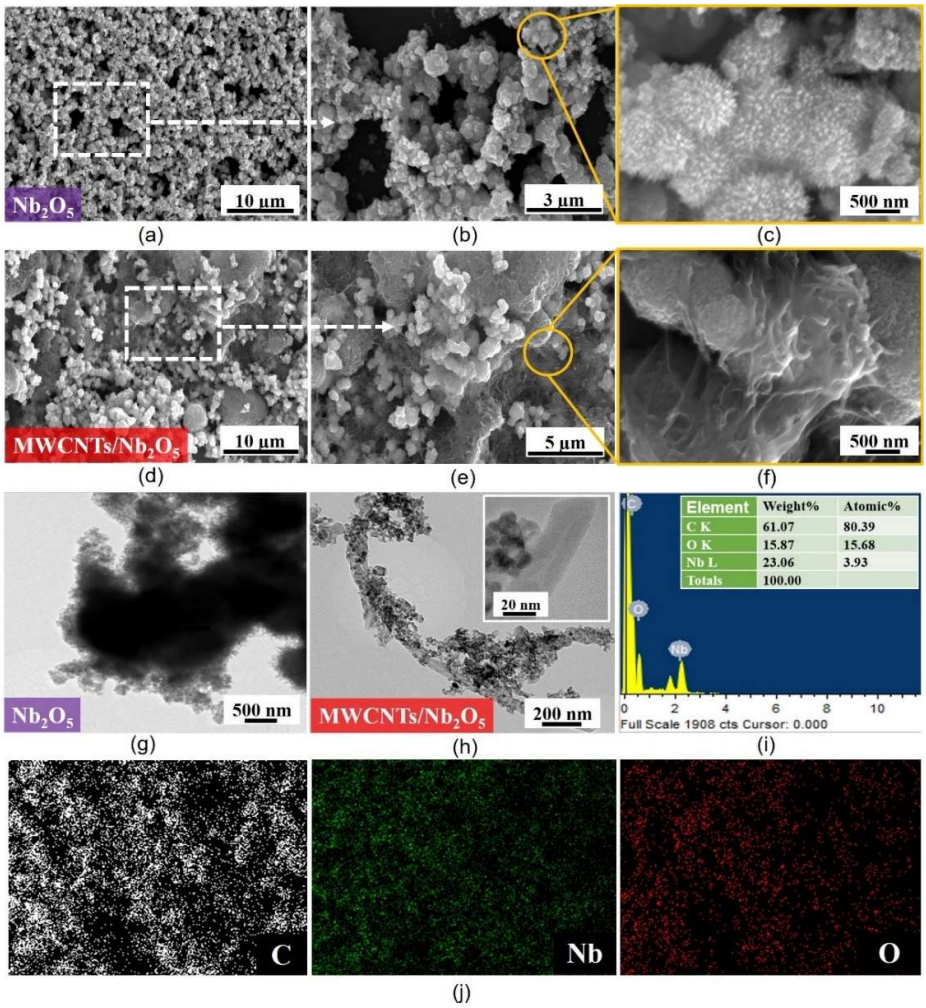


Figure 3.13: Low and High magnification FESEM images of (a-c) Nb_2O_5, (d-f) 1wt% MWCNTs/Nb_2O_5, (g-h) TEM images of Nb_2O_5 and 1 wt% MWCNTs/Nb_2O_5, (i-j) EDS and elemental mapping of 1 wt% MWCNTs/Nb_2O_5

Further, the crystalline phases of Nb_2O_5 and MWCNT/Nb_2O_5 hybrid were characterized by XRD (see Figure 3.14 (a)). The XRD peaks of Nb_2O_5 NPs calcinated at 500˚C show a pseudo-hexagonal structure of Nb_2O_5 NPs with typical peaks at 22.4°, 28.5°, 36.7°, 50.7° and 55.8°. The XRD pattern of the calcined MWCNT/Nb_2O_5 sample exhibited a notable reduction in the amorphous background, suggesting that the crystallinity of the sample increased significantly. This is supported by the appearance of typical peaks corresponding to JCPDS 28–0317 (Murayama et al., 2016; Santos et al., 2023). The synthesis of Nb_2O_5 exhibited a broad absorption spectrum ranging from 200 to 380 nm as depicted in Figure 3.14 (b). The absorption peak's starting wavelength was estimated to be ~280 nm, which corresponds to a band gap energy of 3.2 eV. This finding aligns well with previously reported articles in the literature, highlighting the influence of synthesis methods (Fuchigami and Kakimoto, 2017; Sreethawong et al., 2012). With the increase of 1 wt% of MWCNT, the absorption peak displayed a red shift and the adsorption wavelength region was altered, leading to a decrease in the band gap energy (~2.96 eV) of the MWCNT/Nb_2O_5 hybrid.

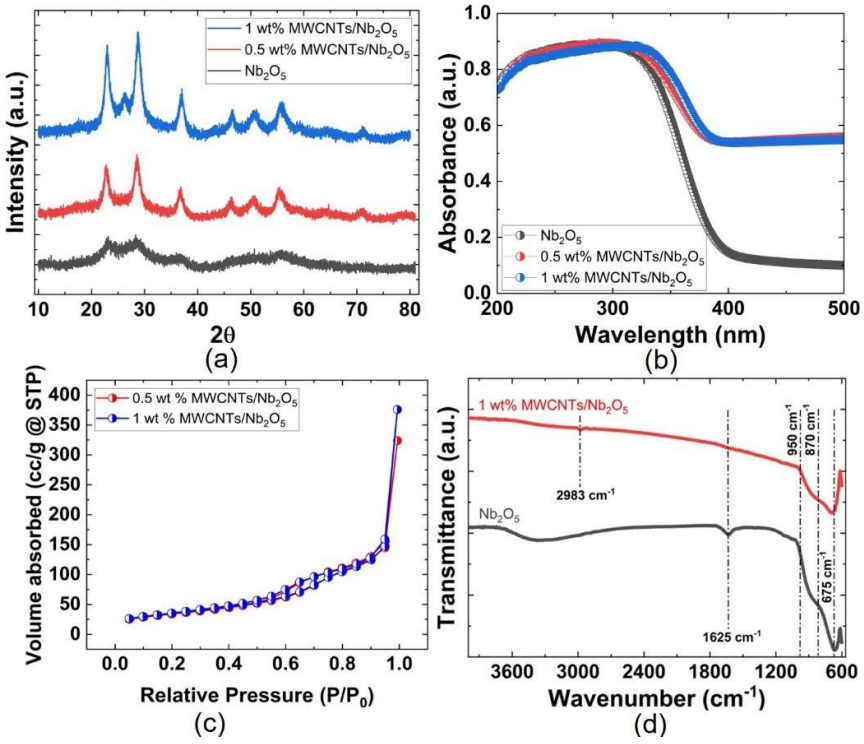


Figure 3.14: (a) XRD, (b) UV-Vis, (c) BET, (d) FTIR spectra of Nb_2O_5 and MWCNT/Nb_2O_5 hybrid

Figure 3.14 (d) displays the FTIR spectra of Nb_2O_5 and MWCNTs/Nb_2O_5 hybrid. The spectrum of the samples mainly consists of a broad shoulder at 675 cm^{-1}, which is attributed to Nb-O-Nb bridges from distorted octahedral NbO_6 (Lopes et al., 2014). Further, a broad band observed between 850 and 970 cm^{-1} is attributed to the stretching of Nb=O groups (Idrees et al., 2019). At 1625 cm^{-1}, a peak can be observed that is attributed to water molecules adsorbed on Nb_2O_5's surface. The FTIR spectra of MWCNTs/Nb_2O_5 display similar peaks, along with two additional distinct bands at 1675 and 2983 cm^{-1} corresponding to C=C and C-H stretching vibrations, respectively from the surface of the nanotubes (Hezam et al., 2020). This finding confirms the development of heterostructure interfaces. XPS was used to analyze the surface chemistry of the synthesized MWCNTs/Nb_2O_5 hybrid (see Figure 3.15 (a)). The XPS survey spectrum of the synthesized hybrid samples shows the presence of Nb, C, and O elements, confirming the high purity of the material. This evidences the decoration of Nb_2O_5 NPs onto the surface of MWCNT. Figure 3.15 (b) displays the C 1s XPS spectra of MWCNTs/Nb_2O_5 with three distinct bonds of C=C, C-C, and C=O peaked at 283.3, 254.7, and 287.3 eV, respectively. As compared to the MWCNT, the binding energies of both the C−O and C=O in the

MWCNTs/Nb_2O_5 composite have shifted to lower energies (Song et al., 2017). This could originate from the interaction between Nb_2O_5 NPs and the oxygenated functional groups of MWCNT. Further, the chemical interaction between MWCNT and Nb_2O_5 NPs is attributed to the construction bonds of Nb-O-C (Yu and Cheng, 2014). The O 1s XPS spectrum of MWCNTs/Nb_2O_5 hybrid shows a peak centered at 530.6 (O−Nb), 531.1 (O=C), and 532.5 eV (O−C), respectively (see Figure 3.15 (c)). In addition, Figure 4.15 (d) shows the Nb 3d spectra with distinct peaks at 207.6 (Nb $3d_{5/2}$) and 210.3 eV (Nb $3d_{5/2}$), respectively, signifying the existence of Nb_2O_5 (Dai et al., 2015).

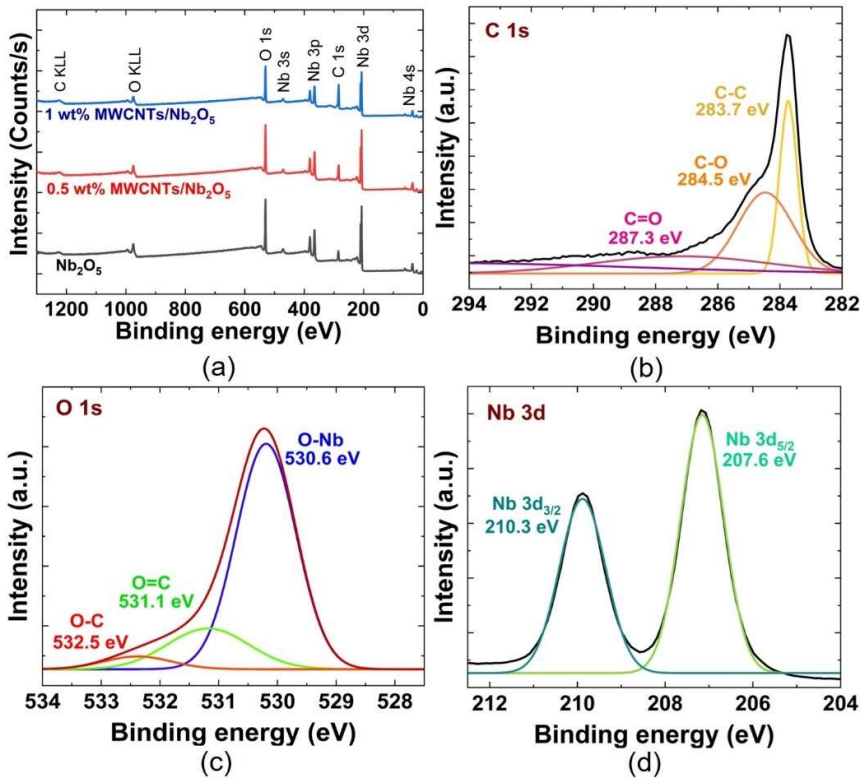


Figure 3.15: XPS results of Nb_2O_5 and MWCNT/Nb_2O_5 hybrid

(b) Gas Sensing Studies

The I–V curves for pristine Nb_2O_5, 0.5 wt%, and 1 wt% MWCNTs/Nb_2O_5 based sensors were measured. The results demonstrate that all sensors display a linear relationship, indicative of an ohmic contact. Notably, the pristine Nb_2O_5 sensor shows a lower current at the same applied voltage compared to the MWCNTs/Nb_2O_5 based devices. This suggests that both MWCNTs/Nb_2O_5 devices exhibit increased conductivity, attributed to the synergistic effects of enhanced specific surface area and the formation of heterojunctions upon MWCNTs addition. Moreover, the high conductivity promotes the adsorption of atmospheric oxygen species on the surface by capturing electrons, thereby improving the sensing performance, particularly for room-temperature gas sensing. All the devices demonstrate good stability and reversibility as shown in Figure 3.16 (a-c), as the response increases rapidly under exposure to different concentrations of gas and returns to its original value upon removal of gas. Further, Figure 3.16 (a) shows the response (%) of Nb_2O_5 device for 5-50 ppm acetone gas at RT. The pristine Nb_2O_5 device shows less response to low concentrations of acetone gas at RT. However, at 50 ppm Nb_2O_5 demonstrated a response of ~1.5%. Further, the addition of 0.5 wt% MWCNTs in Nb_2O_5, resulted in an improvement of detection of acetone gas at RT. With changes in the concentration level of acetone gas, the response of the 0.5 wt% MWCNTs/Nb_2O_5 device increased. The sensor showed a response of ~1.1% at 5 ppm and gradually increased to ~3% at 50 ppm. Further, the 1 wt% MWCNTs/Nb_2O_5 device demonstrated an enhanced response of 1.24% to 3.29% under the exposure of 5 to 50 ppm of acetone gas, respectively.

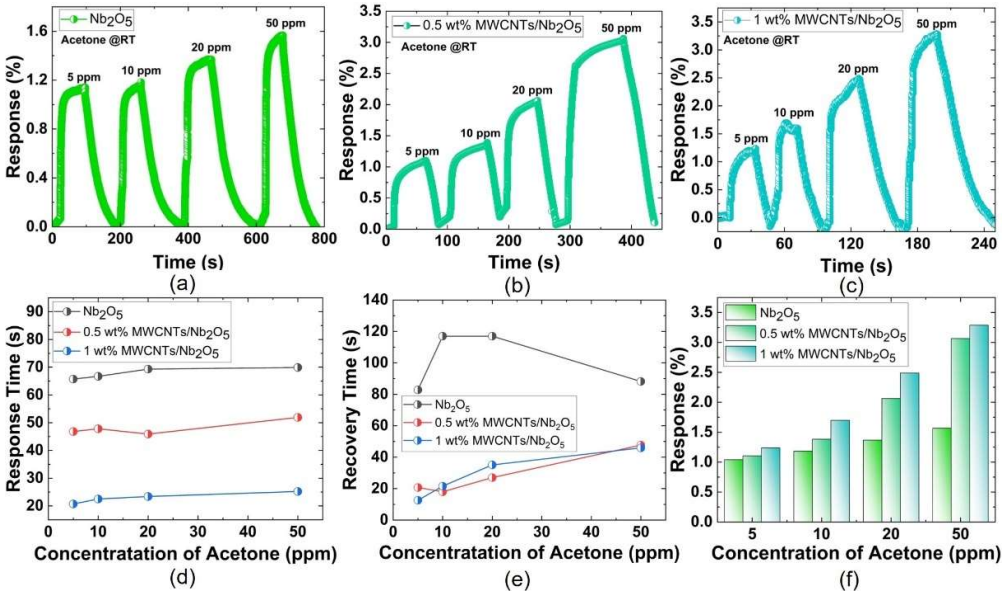


Figure 3.16: Graphs depicting the time-dependent response (%) for (a) Nb_2O_5, (b) 0.5 wt% and (c) 1 wt% MWCNT/Nb_2O_5 hybrid, (d, e) a comparative response/recovery time graph and response (%) for Nb_2O_5 and (0.5 wt% and 1 wt%) MWCNT/Nb_2O_5 hybrid

Figure 3.16 (f) illustrates the comparative response (%) plot of all devices. The results highlight the superior response of the 1 wt% MWCNTs/Nb_2O_5 device at each acetone gas concentration. Further, the device shows ~1.18x (118% higher response by proportion) and ~2.1x (209.9% higher response by proportion) after loading the 1 wt% MWCNTs to pristine Nb_2O_5 device. The impact of adding MWCNT to Nb_2O_5 can be partly explained by considering their work functions: Nb_2O_5 has a work function of ~4.29 eV (Huang et al., 2017), while MWCNTs have a work function of ~4.95 eV (Narjinary et al., 2017). This difference in work function causes electrons to transfer from Nb_2O_5 to MWCNTs at their interface. Additionally, the high surface area of MWCNTs increases their adsorption capacity, thereby enhancing the adsorption ability of the Nb_2O_5 surface when they are combined. As a result, as the gas concentration increases, the response shows an increasing trend. Additionally, Figure 3.16 (d, e) displays the response and recovery times of all devices for acetone gas. The response times to 5 ppm and 50 ppm acetone are nearly the same, 66 s and 70 s, respectively. However, the recovery time shows an opposite trend compared to the response time. This can be explained by the dynamic balance between gas adsorption and desorption. At low concentrations, gas adsorption dominates, taking longer to reach equilibrium, thus resulting in a longer response time. Conversely, at higher concentrations, equilibrium is achieved more quickly, leading to a shorter response time. In our study, we found that the sensor's response time is nearly the same for both 5 ppm and 50 ppm. During the recovery process at room temperature, gas desorption primarily depends on diffusion (Meng et al., 2018), resulting in a generally longer recovery time. Additionally, the response process produces water, which affects gas desorption. Typically, additional heating is required to provide the gas with enough energy for desorption. In our experiments, no heating was applied during the recovery process, so the recovery time is slightly longer than the response time. The results further demonstrate the superiority of the 1 wt% MWCNTs/Nb_2O_5 device, showcasing the fastest response and recovery times compared to other devices. Figure 3.17 (a) illustrates the response and recovery times of the device at 50 ppm acetone, which are 25 sec and 46 sec, respectively.

To evaluate the practicality of the prepared flexible devices, the performance of the 1 wt% MWCNTs/Nb_2O_5 sensor was examined through tests for repeatability, sensitivity, selectivity, and stability. Figure 3.17 (b) depicts the consistency of the sensor when subjected to 50 ppm of acetone gas, as demonstrated in the repeatability test. The results showed that the device's response remained consistent throughout a three-cycle test, indicating stability and potential for practical use. Further, sensitivity was determined by the change in response for every 1 ppm

variation in the target gas concentration, represented by the slope of the linear regression line in Figure 3.17 (c), which is calculated to be 0.0828%/ppm. Using this slope, the sensor's limit of detection (LOD) can be derived with the formula: LOD = 3 × (rms/slope). The root mean square (rms) deviation, computed from the fifth-order polynomial fit of the baseline, was found to be 0.00913 for the 1wt% MWCNTs/Nb_2O_5 sensor (see Figure 3.17 (d)). This results in an LOD of ~330 ppb. In actual use, room-temperature flexible devices must have the ability to differentiate between various gases. The selectivity of the 1 wt% MWCNTs/Nb_2O_5 sensor was subsequently assessed and depicted in Figure 3.17 (e). The relative response (%) for 50 ppm ethanol, methanol, and toluene was found to be ~1.06%, ~0.58%, and ~0.5%, respectively. Acetone elicited a greater response than the other interfering gases that were examined. The results reveal that acetone's response was ~3.29% at 50 ppm due to its strong influence on efficiently removing the adsorbed oxygen on the surface of the MWCNTs/Nb_2O_5 device. Furthermore, the sensor was subjected to a stability test that spanned across a 20-day duration, revealing that the sensor exhibited negligible variation in response (see Figure 3.17 (f)). These results indicate that the device is well suited for applications in environmental, domestic, and healthcare settings.

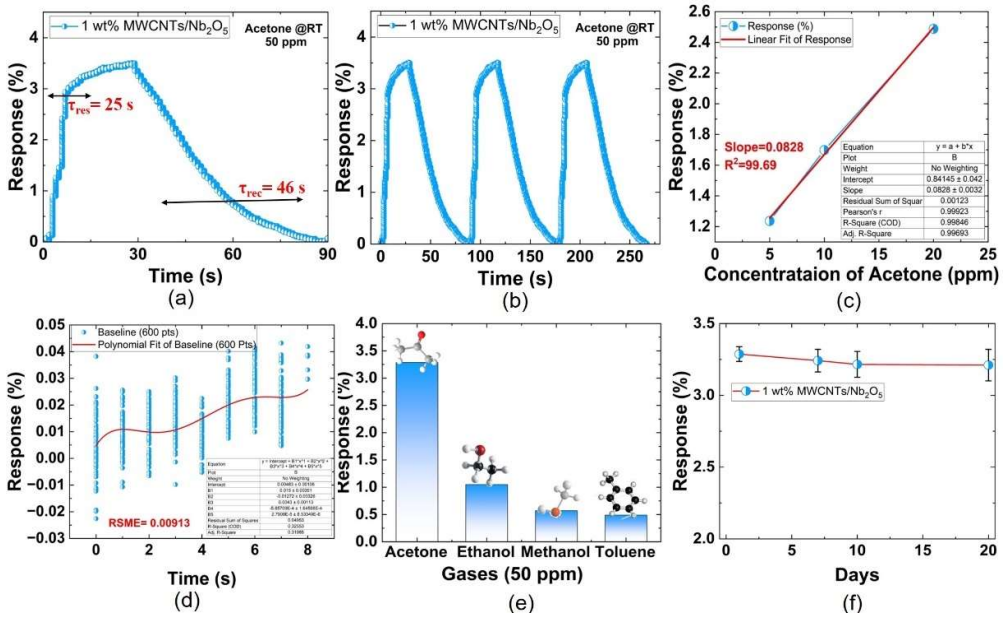


Figure 3.17: (a) Response of 1 wt% MWCNTs/Nb_2O_5 to 50 ppm acetone concentration at RT, (b) Three-cycle repeatability test conducted at 50 ppm acetone, (c, d) Linear regression analysis for sensitivity calculation based on response, and 5th order polynomial fit of baseline, (e) Selectivity, and (f) Stability testing of 1 wt% MWCNTs/Nb_2O_5 evaluated over 20 days at RT

(c) Visualization, Classification, and Predictions of Analytes through ML Algorithms

Before using any ML algorithms, feature extraction is the first stage in preprocessing any sensor signal. a total of 192 data (4 analytes, 4 concentrations, 3 features (response time, recovery time, and response (%)), 4 cycles = 4×4×3×4) were extracted from 1 wt% MWCNTs/Nb_2O_5 sensor for all analytes namely, acetone, ethanol, methanol, and toluene (see Figure 3.18 (a-c)). One effective method to identify sensor data with the highest prediction accuracy is to visualize the data in lower dimensions. A t-SNE method was used to visualize the collected data points. The distinct cluster formation in t-SNE demonstrated that no instances of overlap exist between the many clusters, indicating that the data is classifiable (see Figure 3.18 (a)). Further, this indicates that the selected features can be used for regression and classification of gases.

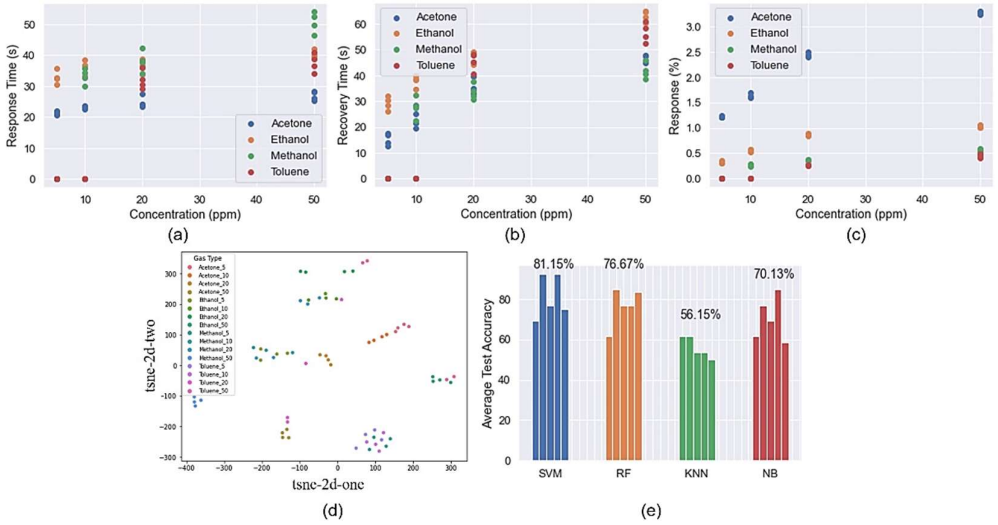


Figure 3.18: (a-c) Extracted feature of sensor for four different gases, namely: acetone, ethanol, methanol, and toluene, (d) t-SNE plots of extracted data points, and (e) Fivefold cross validation test accuracies of the SVM, RF, KNN, and NB algorithms

Four algorithms, specifically SVM, RF, NB, and KNN classifiers, were used in conjunction with the k-fold cross-validation technique to optimize the utilization of the existing data and determine the classification algorithm parameters for the target analyte. K fold cross-validation involves randomly partitioning the original data into k subsamples. Out of these subsamples, k-1 groups are utilized for training, while the remaining group is used for validation. The distribution was iterated k times, resulting in the mean accuracy of all iterations. The classification accuracy for test data in each split of the observed fivefold CV is shown in Figure 3.18 (b). The average test accuracies for SVM, RF, KNN, and NB are 81.15%, 76.67%, 56.15%, and 70.13%, respectively. Since SVM is a maximum margin classifier, i.e., it has an optimal margin gap between separate hyperplanes, resulting in the production of expected test accuracies. Whereas KNN resulted in lower accuracy as there is no learning involved, unlike in the case of SVM and RF.

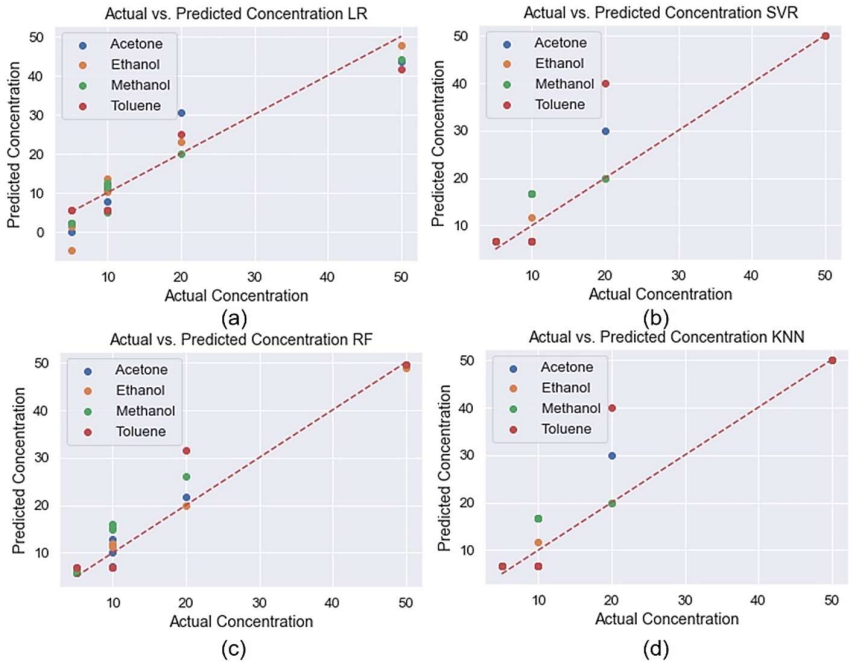


Figure 3.19: (a-d) Gases are quantitatively analyzed using LR, RF, SVM, and KNN regression

For the practical implementation of any desired application, qualitative gas detection alone would not be sufficient. To determine the precise concentration of the gases of interest, regression methods were used following the accurate classification of the gases. To conduct a regression analysis, the entire dataset was segregated into two separate subsets: a training set comprising 60% of the data, and a testing set consisting of 40% of the data, which corresponded to each analyte. The algorithms showed excellent performance in accurately estimating the concentrations of all target analytes. Specifically, the mean absolute error (MAE) values for acetone, ethanol, methanol, and toluene using LR were 27.42, 20.40, 11.86, and 22.85, respectively. Similarly, SVR accurately modelled the datasets, yielding MAE values of 82.13, 39.09, 194.99, and 40.98, respectively. The RF regressor demonstrated a strong fit and accurate prediction, as evidenced by the MAE values of 2.78, 1.87, 17.88, and 23.90 for acetone, ethanol, methanol, and toluene, respectively. Lastly, the KNN regressor was used to train the datasets, resulting in MAE values of 24.60, 9.13, 19.84, and 62.70 for acetone, ethanol, methanol, and toluene, respectively. Figure 3.19 (a-d) shows graphs that illustrate the comparison between the actual data (denoted by dashed diagonal lines) and the predicted data (denoted by symbols) for all analytes. It is evident that the regression models exhibit a high level of accuracy with minimal error at lower concentrations. However, as the concentrations increase, there are deviations from the expected values, indicating a lack of accuracy in the fit.

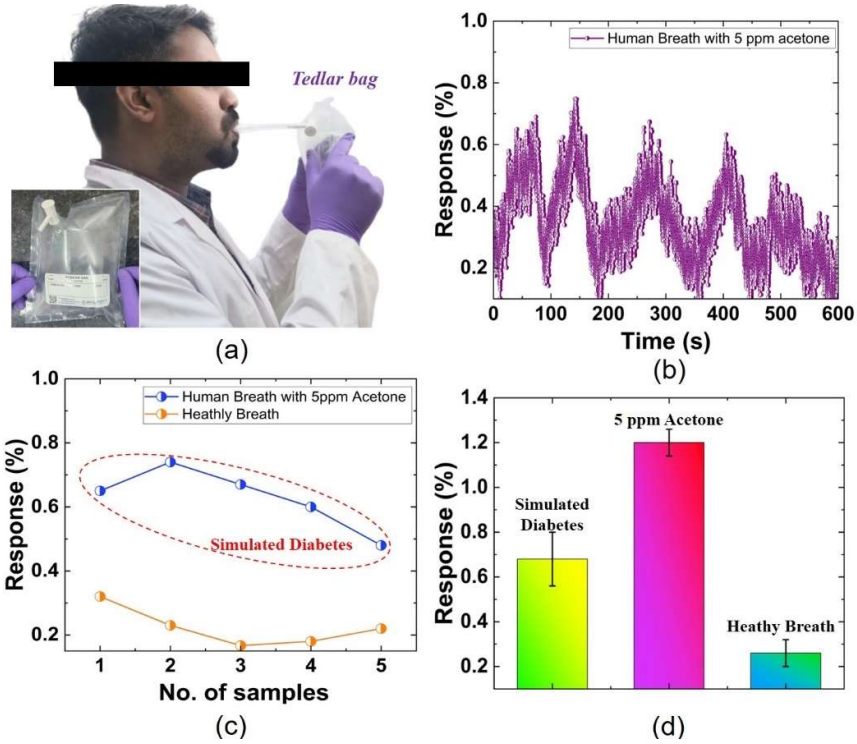


Figure 3.20: (a) Collection of the breath of healthy volunteers in a Tedlar bag, (b) response of the device under the condition of simulated diabetes, where 5 ppm acetone was injected into the collected breath samples from healthy volunteers, (c) response curve of the device for different volunteer samples, distinguishing between healthy and simulated diabetic breath; (d) Comparison of the device responses when exposed to simulated diabetic breath, 5 ppm acetone, and breath from healthy volunteers

We conducted further experiments to examine the potential of a 1 wt% MWCNTs/Nb_2O_5 device for breath analysis, which was attached to a commercially available N95 mask (see inset of Figure 3.21). In our study, a breath of a healthy volunteer was collected in a 1L Tedlar bag and further mixed with acetone (5 ppm) to simulate the breath of diabetic patients (see Figure 3.20 (a)). Figure 3.21 (b, c) illustrates the response (%) of the sensor in the presence of both simulated diabetic and healthy breath environments. Furthermore, the sensor underwent a comparative analysis under exposure to simulated diabetes, 5 ppm acetone, and healthy breath samples. The

results depicted in Figure 3.21 (d) indicate that the sensor's response toward simulated diabetes is less pronounced than its response to pristine acetone (5 ppm), however, it remains significantly higher compared to its response to healthy breath. This capability suggests the potential to distinguish between healthy and diabetic individuals. Therefore, the 1 wt% MWCNTs/Nb_2O_5 sensor exhibits promising prospects for detecting biomarkers in future applications for respiratory diagnosis. Moreover, the comparative analysis of previously developed flexible devices with room temperature acetone gas detection is shown in Table 3.2.

The primary sensing of Nb_2O_5 relies on the changes in resistance resulting from the adsorption and desorption processes, which are caused by the interactions between adsorbed O^{2-} and the target gases on the surface of the sensing layer. Particularly, the sensing performance of MWCNTs/Nb_2O_5 hybrid has shown significant improvements over pristine Nb_2O_5. This could be due to the following factors; firstly, when the MWCNTs/Nb_2O_5 based sensor is exposed to air, oxygen molecules capture electrons from the conduction band of hybrid material, transforming into O^{2-} species at RT. These chemisorbed O^{2-} species form a depletion layer on the MWCNTs/Nb_2O_5 surface, affecting the baseline resistance in air and reacting with the acetone introduced later (Shao et al., 2023). At RT, the interaction between acetone and the adsorbed O^{2-} releases electrons, which are rapidly transferred through the conductive channels formed by the Nb_2O_5 and MWCNTs interface (C. Li et al., 2023). This promotes further reactions with the acetone, thereby enhancing the sensor's response. The involved chemical interaction between acetone and absorbed O^{2-} is presented in Figure 3.21. Further, the improved sensing characteristics of the MWCNTs/Nb_2O_5 hybrid are attributed to enhanced resistance modulation due to the p-type doping of MWCNTs and the formation of a p-n heterojunction between MWCNTs and Nb_2O_5. Secondly, there is a substantial morphological transformation. For instance, the urchin shaped Nb_2O_5, when evenly coated on the exterior of the MWCNTs, improves the specific surface area (as confirmed by the BET as shown in Figure 3.14 (c)) and conductivity of the hybrid material. Furthermore, the ability of the MWCNTs/Nb_2O_5 to absorb O^{2-} and offer numerous active sites for interacting with acetone gas is enhanced by their larger surface area and reduced tendency to aggregate particles.

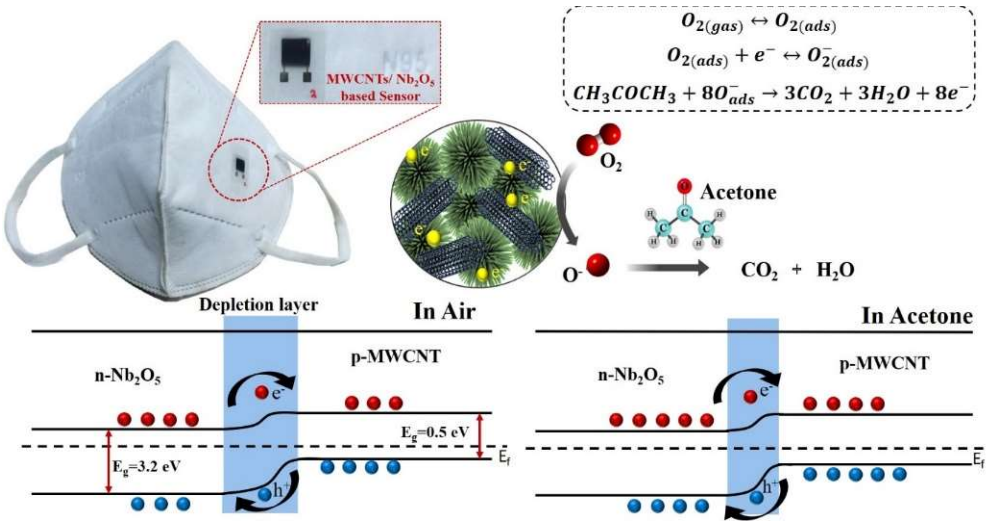


Figure 3.21: Sensing mechanisms of MWCNTs/Nb_2O_5 based sensor with inset photograph of an N95 Mask attached to a flexible acetone sensor

Table 3.2: Comparative analysis of acetone-based sensors operating at RT

Material	Temp. (°C)	Response (%)	τ_{res} (s)	τ_{rec} (s)	LOD
Ag@CNT (Young et al., 2020)	RT	~1.64 (100 ppm)	13	10	50 ppm

NiO-WO_3 (Choi et al., 2017)	300	4.4 (200 ppm)	51	59	5 ppm
rGO-Se (Hussain Shar et al., 2020)	135	3.2 (100 ppm)	13	10	25 ppm
$ZnFe_2O_4$-GQDs (Chu et al., 2019)	RT	3.2 (100 ppm)	11	4	5 ppm
MWCNTs/Nb_2O_5 (This Work)	RT	~3.28 (50 ppm)	26	45	330 ppb

3.2.4 Summary

The study demonstrated the fabrication of a flexible MWCNTs/Nb_2O_5 based breath sensor for detecting acetone at ambient temperature. The results of the structural and morphological experiments indicated the successful synthesis of a sensing material, which was then coated onto a flexible PET substrate to fabricate the breath sensing devices. Furthermore, the prepared sensor with 1 wt% MWCNTs/Nb_2O_5 demonstrated fast response/recovery times of 26/45 sec, respectively, as well as reliable stability, selectivity, and detection limit of 330 ppb for acetone gas. Furthermore, characteristic features were extracted from the breath sensor. Various ML algorithms were used to visualize, classify, and predict the tested analyte with good quantifications. In addition, the sensor demonstrated its ability to effectively distinguish between healthy and simulated diabetic breath samples. The presented results indicate the significant potential of this breath sensor for detecting acetone in both environmental and human breath samples.

...